Nernst coefficient of Pt by non-local electrical measurement

Tony Chiang ⓘ ; Johanna Nordlander ⓘ ; Julia A. Mundy ⓘ ; John T. Heron ✉ ⓘ

Check for updates

View Online   Export Citation

17 April 2024 01:07:37

Nernst coefficient of Pt by non-local electrical measurement

View Online   Export Citation   CrossMark

Tony Chiang,[1] (iD) Johanna Nordlander,[2] (iD) Julia A. Mundy,[2] (iD) and John T. Heron[1,a] (iD)

AFFILIATIONS

[1]Department of Material Science and Engineering, University of Michigan, Ann Arbor, Michigan 48109, USA
[2]Department of Physics, Harvard University, Cambridge, Massachusetts 02138, USA

[a]Author to whom correspondence should be addressed: jtheron@umich.edu

ABSTRACT

The Nernst effect describes a linear relationship between orthogonal components of a magnetic field, a temperature gradient, and a resulting transverse electric field. A non-local electrical measurement, where injection and detection are physically separated on the specimen, serves as a versatile and effective platform for measuring spin and thermal effects due to the avoided interference with a charge current directly. Here, we quantify the Nernst coefficient of Pt, a common material for spin injection in non-local geometries, by a non-local electrical measurement under modulated temperature and magnetic field and finite element analysis for modeling heat transfer. We determine the Nernst coefficient of Pt from room temperature ($8.56\,\text{nV}\,\text{K}^{-1}\,\text{T}^{-1}$) to 10 K ($29.3\,\text{nV}\,\text{K}^{-1}\,\text{T}^{-1}$). Beyond the quantification of the Nernst coefficient, our results show that careful consideration of the thermal properties of the thermal sink and electrode materials is needed when making an interpretation of non-local electrical measurements.

First discovered in the 1880s by Walther Nernst and Albert von Ettingshausen, the Nernst–Ettingshausen (Nernst, commonly) effect occurs when a thermal gradient present in a material drives a flow of charge current. When together with a perpendicular magnetic field, the electron trajectory curves via the Lorentz force create a transverse electric field, similar to the mechanism of the Hall effect. The Nernst effect is expressed as

$$E_i = \upsilon_{ijk}\partial_j T B_k, \tag{1}$$

with $i, j, k = x, y, z$. Here, E_i is the resulting electric field generated by the Nernst effect, υ_{ijk} is the Nernst tensor (third rank, axial), $\partial_j T$ is the applied thermal gradient, and B_k is the applied magnetic field. For the Nernst effect to be non-zero, the vectors E_i, $\partial_j T$, B_k must have orthogonal components (when considering materials of high symmetry) such that $i \neq j \neq k$. Thus, for isotropic media, the Nernst coefficient is expressed as[1–4]

$$\nu = \frac{E_y}{B_z}\frac{1}{\partial_x T}. \tag{2}$$

In the non-local measurement geometry, two conducting strip electrodes are patterned on an insulating substrate, one electrode serves as the injector of heat, while the other serves as the detector (Fig. 1).

However, multiple effects could take place in such geometry depending on the materials and the signals source/measured and a careful examination will require evaluation of the symmetry of the spin, thermal, and magnetothermal signals for accurate interpretation. For example, a spin current could be generated from platinum via the spin Hall effect, and the spin current could propagate into the insulating substrate, then into the detector, and read as a voltage via the inverse spin Hall effect.[5] This provides an opportunity to study the injection and transport of spin in the substrate material. However, thermal effects can also be measured by resistive (Joule) heating of the injector electrode from the applied injection current.[6–8] The injected heat can propagate to the detector electrode and read through a change in voltage and provide a unique geometry for measuring thermal properties involving thermal gradients, such as the (anomalous) Nernst effect.

In this work, we investigate the Nernst effect of a thin platinum strip from 3 to 300 K in this non-local geometry. In this case, the heat is generated via Joule heating by the injection of a DC charge current into the injector strip which is then injected into the substrate (Fig. 1). The heat then diffuses across the strip detector electrode separated from the injector electrode by a distance d and creates a thermal gradient across the width of the detector electrode. In the presence of a magnetic field perpendicular to the temperature gradient, a transverse
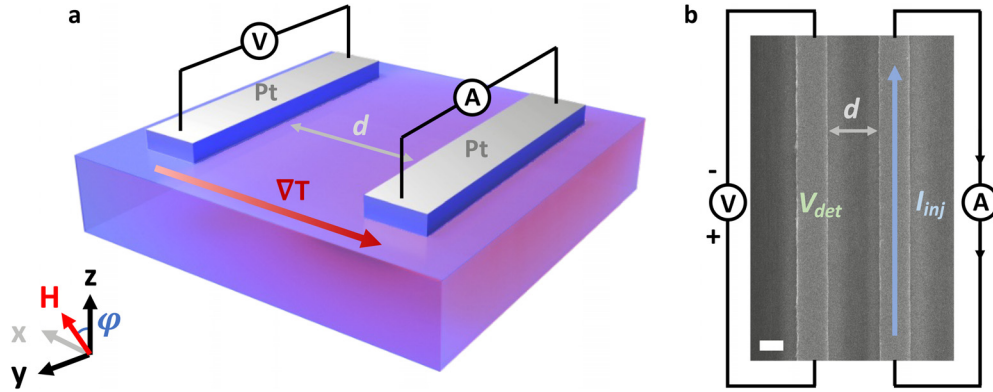
FIG. 1. Device geometry and measurement setup. (a) Schematic of the device, with two patterned platinum strips with a thickness of 15 nm deposited on top of a (111)-oriented single crystal YSZ substrate with a variable spacing d. One serves as an injector of heat through Joule heating from an applied DC, while the other serves as a signal detector with voltage readout. The generated heat at the injector propagates to the detector, resulting in a temperature gradient across the width of the detector strip. An external magnetic field is applied at an angle φ with respect to the z-axis within the x–z plane. (b) Scanning electron microscopy image of a device with a d spacing of 600 nm. The spacing d ranges from 100 nm to 1 μm while keeping the width of the Pt strips fixed at 350 nm. The lower left scale bar represents 300 nm.

electric field emerges in the detector electrode. YSZ (Y_2O_3 stabilized ZrO_2, 8 mol % Y_2O_3) and MgO substrates are used to tune the thermal gradient and the resulting Nernst signal. Together with finite element analysis for modeling heat flow and temperature dependent thermometry measurements, we determine the Nernst coefficient of Pt from room temperature (8.56 nV K^{-1} T^{-1}) to 10 K (29.3 nV K^{-1} T^{-1}).

Our sample is the device in Fig. 1 fabricated on a (111)-oriented yttria-stabilized zirconia (YSZ) single crystal substrate with dimensions of $5 \times 5 \times 0.5$ mm^3. Our measurements track V_p and V_n, the detector voltage at positive injection current and negative injection current, respectively. Then the signal at the detector electrode is separated into symmetric and asymmetric components defined as follows:

$$V_{sym} = V_p - V_n,$$
$$V_{asym} = V_p + V_n.$$

Here, V_{sym} represents the non-thermal-related contribution since the subtraction excludes the thermal signal which does not vary with the polarity of the injection current ($\propto I_{inj}^2$). On the contrary, the V_{asym} term isolates the thermal contributions. The amplitudes of the signals can be extracted by a first-order fit for V_{sym} and a second-order fit for V_{asym} when expressed as functions of the injector current

$$V_{sym} = I_{inj}R_1,$$
$$V_{asym} = I_{inj}^2 R_2.$$

The first-order coefficient R_1 is the effective resistance of the linear signal, while the second-order coefficient R_2 originates from Joule heating where the power is proportional to I_{inj}^2 and encompasses the amplitude of the thermal signal. For interpreting the signal, a thorough analysis of the possible effects needs to be considered.

First, magnon transport has been demonstrated in magnetic systems[1,2,9–12] Magnons can be excited by injecting spin with a heavy metal injector (such as Pt or W) via the spin Hall effect, and the excited magnons can then propagate to the detector where the magnon spin is converted back to a charge current by the inverse spin Hall effect. This is solely a first-order effect with no thermal contribution and can be excluded if the observed signal is only a second-order signal.

Next, the spin Seebeck effect arises from a temperature gradient across the separation distance between injector and detector electrodes, inside the substrate or film, driving a spin current (or magnon) toward the detector. Excited thermally, this is a second-order effect as the heating power is proportional to I_{inj}^2. It has been experimentally observed in ferromagnet and antiferromagnet materials using the non-local geometry with an applied in-plane magnetic field.[3,13–17] In a ferromagnet, the spin Seebeck signal would be nonlinear with magnetic field and eventually saturate as the field strength surpasses the coercive field. In an antiferromagnet, the spin Seebeck would show nonlinearity and saturation with field but typically at much higher field strengths. Furthermore, recent investigation of spinon transport reported by means of the spin Seebeck effect in the proposed quantum spin liquid system seem promising,[18] yet, in this particular system, the reported signature of the spin Seebeck effect has a linear dependence on field that closely resembles the Nernst effect. Hence, a careful examination is needed such as control measurements to help us clarify the results.

Finally, the Nernst effect would occur in the non-local geometry from the temperature gradient across the width of the detector strip, contrary to the spin Seebeck effect where the signal is generated from the temperature gradient across the region between the injector and detector electrodes. One distinctive feature that can be used to discern the two is the orientation of the magnetic field. The Nernst effect requires the magnetic field to be orthogonal to the temperature gradient, and therefore, oriented out-of-plane.

We first confirm the properties of our Pt electrodes with temperature and field-dependent resistance measurements of the injector strip [Fig. 2(a)]. Conventional metallic behavior, negligible magnetoresistance (field is normal to the sample surface), and linear I(V) (inset) curves are observed. Contrary to this, Fig. 2(b) shows the raw detector voltage, V_{det}, where a clear parabolic dependence on the injection current and monotonic magnetic field dependence is observed. The V_{asym} signal [Fig. 2(c)] further highlights the thermal contribution where the second-order fit is in good agreement. The magnetic field dependence of V_{asym} matches well with the Nernst effect as the signal is proportional to the magnetic field and vanishes at zero field. Furthermore, the symmetry of the field dependence matches that of the Nernst effect.
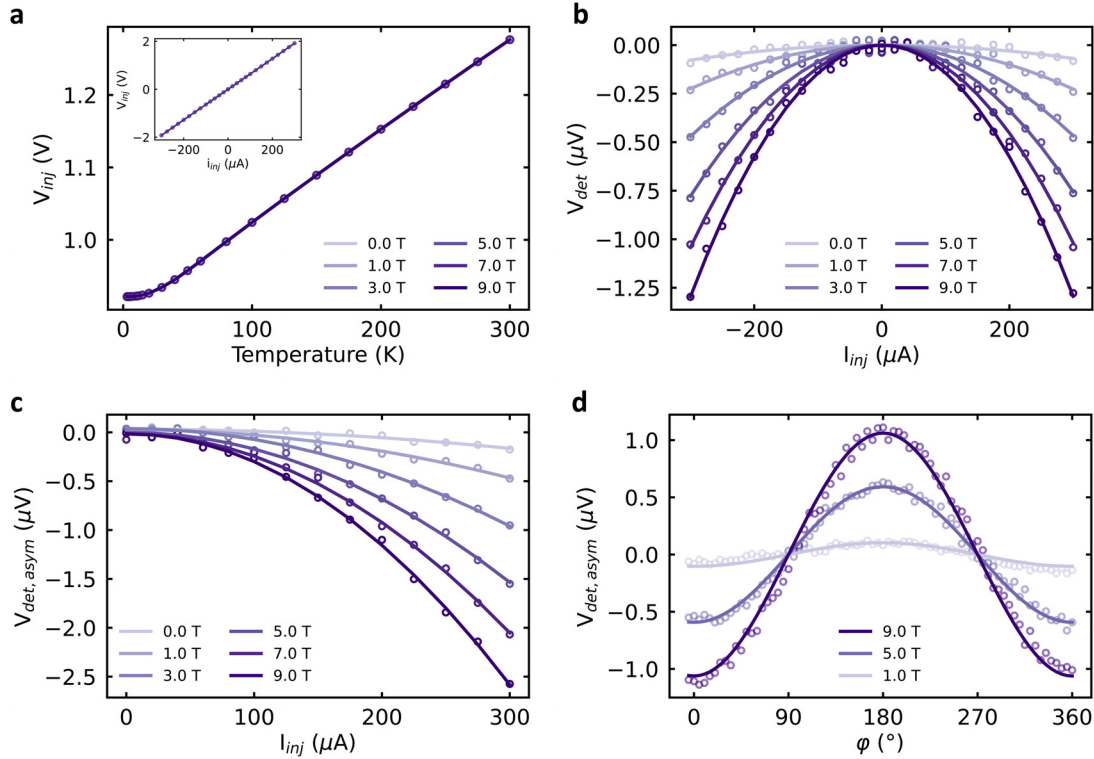
FIG. 2. Symmetry of the non-local electrical measurements as a function of the injection current. (a) Injector voltage as a function of temperature with an applied current of 200 μA, measured at multiple magnetic field strengths (up to 9 T) and oriented along the z-axis with the YSZ substrate. A negligible magnetoresistance, below 0.04%, is observed. The inset shows the I_{inj}–V_{inj} signal up to 300 μA at 300 K, revealing Ohmic behavior. (b) Non-local electrical measurements as a function of I_{inj}, measured on a device with 400 nm spacing at 300 K and with magnetic field applied along the z-axis. The hollow circles are raw signals measured on the detector strip as a function of I_{inj} at various magnetic fields and fitted to a second-order equation that is shown by the solid line. The signal is dominantly quadratic and consistent with a thermal effect. (c) Asymmetric detector signal, isolating the heat-related effect. The hollow circles represent the measured data while the solid lines are the second-order fit. (d) Magnetic field rotational scan along φ at 300 K with an injection current of 200 μA and 400 nm gap. A background signal that is independent of field has been removed. The rotational scan has a $-\cos \varphi$ dependence consistent with the symmetry of the Nernst effect.

Figure 2(d) shows the rotational dependence of V_{asym} with different magnetic field strengths. A $\cos(\varphi)$ dependence is observed, with the signal showing a maximum (minimum) when the magnetic field is applied out-of-plane. A constant background signal (thermovoltage) has been removed.

To further evaluate this magnetothermal effect, the R_2 values were extracted from the injection current sweeps at various out-of-plane field strengths [Figs. 3(a) and 3(b)]. R_2 shows a linear dependence in agreement with the Nernst effect and with no sign of saturation or non-linearity that is normally observed in magnon and spin Seebeck transport in magnetic media. YSZ has a low thermal conductivity (2.4 W m^{-1} K^{-1}),[19] to investigate the role of the thermal properties of the underlying substrate on the Nernst signal; we also perform comparative measurements on a (001)-oriented magnesium oxide (MgO) single crystal substrate [thermal conductivity = 45 W m^{-1} K^{-1} (Ref. 20)] that has the same dimensions as the YSZ crystal. Consistent with the higher thermal conductivity, and thus, smaller thermal gradient across the detector electrode, Fig. 3 reveals a small (negligible) signal observed for the MgO sample. Finally, the measurement was conducted with a wide range of temperatures, from 3 to 300 K. The R_2 magnitude decreases with decreasing temperature approximately linearly until ∼20 K.

To understand this temperature behavior and quantify the Nernst coefficient, the changes in thermal properties of the substrate need to be taken into account. This is studied by tracking the temperature of the detector while heating up the injector. The detector temperature was evaluated from the temperature dependent resistance of the platinum wire. Figure 4(a) shows a clear temperature rise of the detector upon injecting current, with higher temperatures observed for the smaller device gaps, verifying the effectiveness of this thermometry probe.

For quantifying the Nernst coefficient, the thermal gradient across the platinum strip is a prerequisite. We compute this with finite element analysis. Our analysis makes use of the stationary study with the AC/DC module for modeling the Joule heating and heat transfer module for analyzing the temperature field, and our device geometry with the material's properties is listed in Methods. The fidelity of the model can be seen in Fig. 4(a), showing a good match between the measured detector temperature and the simulated value with less than 0.1% difference. Next, the temperature difference ΔT across the width of the detector is computed as a function of spacing distance, for both the YSZ and MgO substrates shown in Fig. 4(b). The results confirm a much larger thermal gradient generated when the YSZ substrate is

17 April 2024 01:07:37
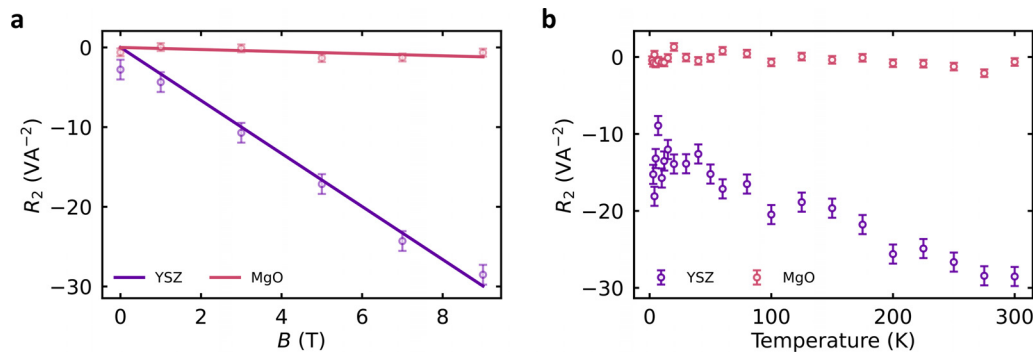
FIG. 3. Extraction of the thermal signal. (a) Amplitude of the second-order signal measured at 300 K measured with spacing d of 400 nm, plotted as a function of the out-of-plane magnetic field. The solid line is a linear fit, here revealing that the second-order signal amplitude has a linear field dependence. The signal for the MgO sample is much lower than that for the YSZ sample, consistent with the lower thermal gradient generated due to the higher thermal conductivity of MgO. (b) Amplitude of the second-order signal measured with a 9 T out-of-plane field from 3 to 300 K, measured with spacing d of 400 nm. The error bars represent one standard deviation.
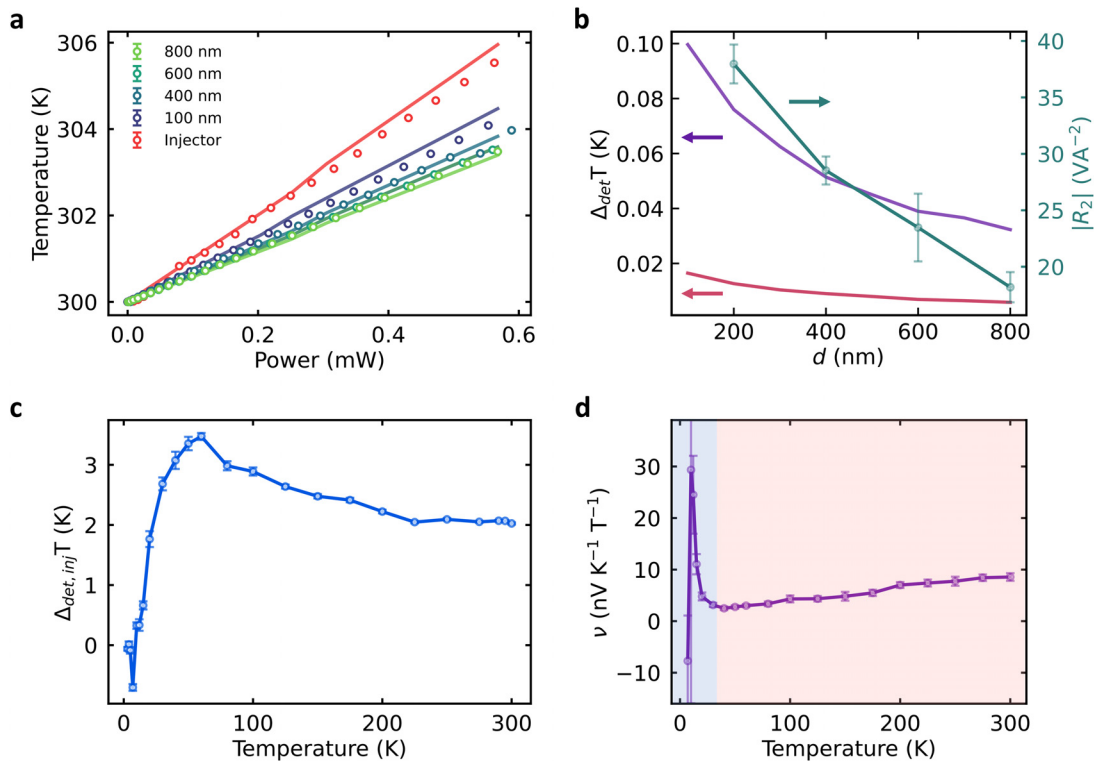
FIG. 4. Analysis of heat transfer and determination of the Nernst coefficient of Pt. (a) Thermometry measurements (hollow circles) and simulations (solid lines) of the injector and detector temperature with various injection powers ($R_{inj}I^2_{inj}$) at 300 K. Excellent agreement is made between the simulation and experimental results (difference is less than 0.1%). (b) Simulation of the temperature difference across the width of the detector platinum strip for both YSZ (purple solid line) and MgO (pink solid line) substrate at various d spacings with an injection current of 200 μA at 300 K. A significantly lower temperature gradient for the MgO sample on account of the differences in thermal conductivity. The right vertical axis shows the experimental d spacing dependence of the R_2 signal from YSZ at 300 K and 9 T, showing an increase in amplitude with decreasing spacing consistent with simulations. (c) Temperature difference of the detector strip in the heated state (200 μA = I_{inj}) and non-heated state (0 μA = I_{inj}) acquired from the thermometry measurement of the YSZ sample as a function of temperature. Trend is consistent with bulk thermal conductivity behavior and room temperature values agree with prior bulk reports (2.4 W m^{-1} K^{-1}). (d) Temperature dependence of the Nernst coefficient of Pt from 3 to 300 K evaluated with a 400 nm spacing device on the YSZ substrate. The red-shaded area indicates a region with a standard deviation error of less than 4 nV K^{-1} T^{-1}, whereas the blue-shaded area has a higher standard deviation error due to the noisy temperature probe at lower temperatures.

used compared with the MgO substrate, in agreement with the scaling of measured R_2 values for the samples on the two substrates. Note that the scaling of R_2 for the MgO sample is smaller than expected for the given temperature gradients of the YSZ and MgO samples. We attribute the lower R_2 values for the MgO relative to simulations to an appreciable interface thermal resistance, which can be significant at interfaces between thin metals and oxides.[21,22] Furthermore, MgO is well known to form hydroxylates on its surface when exposed to water, complicating the atomic scale structure of the interface.[23] The simulations shown in Figs. 4(a) and 4(b) are done without interface resistance and agree well with the data for the YSZ sample. The agreement is not as strong for the MgO sample as shown in the supplementary material, Fig. S1(a). Much better agreement is achieved when adding interfacial thermal resistance of $2 \times 10^{-8}\,\mathrm{K\,m^2\,W^{-1}}$ (comparable in size to many other oxide metal interfaces[24]). The additional resistance lowers the detector temperature, and more importantly, the temperature profile of the detector [supplementary material, Fig. S1(b)]. The temperature difference across the detector goes from 0.009 K without interfacial thermal resistance to $\sim$0.002 69 K with interfacial thermal resistance, revealing a more than 3$\times$ reduction in the temperature gradient in agreement with the R_2 data in Fig. 3(b).

In addition, the R_2 signal is tracked at multiple spacing distances, from 200 to 800 nm shown in Fig. 4(b). The difference in spacing leads to a different thermal gradient across the detector width, which agrees with the trend from simulation.

The thermometry measurement was conducted as a function of temperature to estimate the change in the temperature gradient. Figure 4(c) shows the measured temperature difference of the detector between the heated state ($I_{inj} = 200\,\mu A$) and non-heated state ($I_{inj} = 0\,\mu A$), exhibiting a similar temperature dependence to the thermal conductivity, implying that the temperature gradient is strongly affected by thermal conductivity. With this, $\partial_x T$ was estimated using the simulated value at 300 K, then calibrated according to the thermometry probe [Fig. 4(c)]. Finally, putting together the thermal gradient obtained from the simulation work and the electrical measurements leads us to the Nernst coefficient of platinum, shown in Fig. 4(d). This reveals a small temperature dependent region above 30 K (with value of $3.14\,\mathrm{nV\,K^{-1}\,T^{-1}}$ at 30 K) and a sudden increase below that temperature. The high temperature regime (40–300 K) fits well to a linear function with a slope of $24.79 \pm 0.989\,\mathrm{pV\,K^{-1}\,T^{-2}}$ and y-intercept of $1.491 \pm 0.176\,\mathrm{nV\,K^{-1}\,T^{-1}}$. The Nernst coefficient can also be obtained using different spacing d shown in the supplementary material, Fig. S2, where a variation of less than 10% is observed, suggesting an accurate evaluation.

Finally, we corroborate our experimentally determined value with an estimate from bulk material parameters for Pt and compare to values for metals in the literature. The Nernst coefficient varies greatly with the type of materials, with values in the range of $0–10\,\mu\mathrm{V\,K^{-1}\,T^{-1}}$ for many metals,[25] to extremely large values reported for semimetal bismuth (above $1\,\mathrm{mV\,K^{-1}\,T^{-1}}$).[26,27] Other reported values include $180\,\mathrm{nV\,K^{-1}\,T^{-1}}$ (20 K) for gold and $900\,\mathrm{nV\,K^{-1}\,T^{-1}}$ (20 K) for copper.[25] Yet, the Nernst coefficient for key materials, specifically, materials with strong spin–orbit coupling that are commonly used in spin transport measurements (platinum and tungsten), is missing.

An alternative expression for the Nernst coefficient for metals in terms of physical parameters is[28,29]

$$\nu = \frac{\pi^2}{3}\frac{k_B}{e}\frac{k_B T}{\epsilon_F}\mu. \qquad (3)$$

Here, the Nernst coefficient is expressed with the Fermi energy, ϵ_F, and the carrier mobility, μ. A direct link to the Seebeck coefficient can be established by rearranging equation (3). First, knowing the Seebeck coefficient for metallic systems is often expressed as

$$S = \frac{\pi^2}{2}\frac{k_B}{e}\frac{T}{T_F}. \qquad (4)$$

Combing Eqs. (3) and (4), the Nernst coefficient can finally be expressed as

$$\nu = \frac{2}{3}S\mu. \qquad (5)$$

This expression implies that the Nernst coefficient is proportional to the product of the Seebeck coefficient and mobility. This provides a convenient estimation of the Nernst coefficient; however, this relation only holds for the one-band system, relying on the assumption of a linear dependence of the Hall angle, $\tan\theta_H$, on energy. However, from Eq. (5), the Nernst coefficient of platinum can be estimated from the bulk Seebeck coefficient $5\,\mu\mathrm{V\,K^{-1}}$ and mobility $9.95\,\mathrm{cm^2\,V^{-1}\,s^{-1}}$,[30,31] with a value of $3\,\mathrm{nV\,K^{-1}\,T^{-1}}$ and in reasonable agreement with our measured value.

In this work, we determine a clear magnetothermal signal in a non-local geometry, with two platinum strips with a thickness of 15 nm patterned on YSZ and MgO substrates. We confirmed the signal is attributed to the Nernst effect based on a systematic analysis, with the field and angular dependence matching the signatures of the Nernst effect. Together with the simulation work, we determined the Nernst coefficient for platinum at room temperature and below. Our work provides guidance for identifying various effects that could occur in such a configuration. In addition, we demonstrated a convenient approach for studying the Nernst effect in thin film where this work can be further extended and applied for heat transport.

See the supplementary material for methods and extended data.

AUTHOR DECLARATIONS
Conflict of Interest

The authors have no conflicts to disclose.

Author Contributions

Tony Chiang: Conceptualization (equal); Data curation (equal); Formal analysis (equal); Investigation (equal); Writing – original draft (equal); Writing – review & editing (equal). **Johanna Nordlander:** Conceptualization (equal); Writing – review & editing (supporting). **Julia A. Mundy:** Conceptualization (equal); Funding acquisition (equal); Project administration (equal); Writing – review & editing (supporting). **John T. Heron:** Conceptualization (equal); Formal analysis (equal); Funding acquisition (equal); Investigation (equal); Project administration (equal); Writing – original draft (equal); Writing – review & editing (equal).

DATA AVAILABILITY

The data that support the findings of this study are available from the corresponding author upon reasonable request.

REFERENCES

[1]J. Gückelhorn, S. de-la-Peña, M. Grammer, M. Scheufele, M. Opel, S. Geprägs, J. C. Cuevas, R. Gross, H. Huebl, A. Kamra, and M. Althammer, "Observation of nonreciprocal magnon Hanle effect," Phys. Rev. Lett. **130**, 216703 (2023).

[2]J. Han, P. Zhang, Z. Bi, Y. Fan, T. S. Safi, J. Xiang, J. Finley, L. Fu, R. Cheng, and L. Liu, "Birefringence-like spin transport via linearly polarized antiferromagnetic magnons," Nat. Nanotechnol. **15**(7), 563–568 (2020).

[3]K. Uchida, S. Takahashi, K. Harii, J. Ieda, W. Koshibae, K. Ando, S. Maekawa, and E. Saitoh, "Observation of the spin Seebeck effect," Nature **455**(7214), 778–781 (2008).

[4]R. Lebrun, A. Ross, S. A. Bender, A. Qaiumzadeh, L. Baldrati, J. Cramer, A. Brataas, R. A. Duine, and M. Kläui, "Tunable long-distance spin transport in a crystalline antiferromagnetic iron oxide," Nature **561**(7722), 222–225 (2018).

[5]J. E. Hirsch, "Spin Hall effect," Phys. Rev. Lett. **83**(9), 1834–1837 (1999).

[6]P. Krzysteczko, J. Wells, A. Fernández Scarioni, Z. Soban, T. Janda, X. Hu, V. Saidl, R. P. Campion, R. Mansell, J.-H. Lee, R. P. Cowburn, P. Nemec, O. Kazakova, J. Wunderlich, and H. W. Schumacher, "Nanoscale thermoelectrical detection of magnetic domain wall propagation," Phys. Rev. B **95**(22), 220410 (2017).

[7]J. Wells, E. Selezneva, P. Krzysteczko, X. Hu, H. W. Schumacher, R. Mansell, R. Cowburn, A. Cuenat, and O. Kazakova, "Combined anomalous Nernst effect and thermography studies of ultrathin CoFeB/Pt nanowires," AIP Adv. **7**(5), 055904 (2017).

[8]P. Krzysteczko, X. Hu, N. Liebing, S. Sievers, and H. W. Schumacher, "Domain wall magneto-Seebeck effect," Phys. Rev. B **92**(14), 140405 (2015).

[9]L. J. Cornelissen, J. Liu, R. A. Duine, J. B. Youssef, and B. J. van Wees, "Long-distance transport of magnon spin information in a magnetic insulator at room temperature," Nat. Phys. **11**(12), 1022–1026 (2015).

[10]C. Liu, Y. Luo, D. Hong, S. S.-L. Zhang, H. Saglam, Y. Li, Y. Lin, B. Fisher, J. E. Pearson, J. S. Jiang, H. Zhou, J. Wen, A. Hoffmann, and A. Bhattacharya, "Electric field control of magnon spin currents in an antiferromagnetic insulator," Sci. Adv. **7**(40), eabg1669 (2021).

[11]T. Wimmer, A. Kamra, J. Gückelhorn, M. Opel, S. Geprägs, R. Gross, H. Huebl, and M. Althammer, "Observation of antiferromagnetic magnon pseudospin dynamics and the Hanle effect," Phys. Rev. Lett. **125**(24), 247204 (2020).

[12]K. Oyanagi, S. Takahashi, L. J. Cornelissen, J. Shan, S. Daimon, T. Kikkawa, G. E. W. Bauer, B. J. van Wees, and E. Saitoh, "Spin transport in insulators without exchange stiffness," Nat. Commun. **10**(1), 4740 (2019).

[13]H. Adachi, K. Uchida, E. Saitoh, and S. Maekawa, "Theory of the spin Seebeck effect," Rep. Prog. Phys. **76**(3), 036501 (2013).

[14]S. M. Wu, W. Zhang, A. KC, P. Borisov, J. E. Pearson, J. S. Jiang, D. Lederman, A. Hoffmann, and A. Bhattacharya, "Antiferromagnetic spin Seebeck effect," Phys. Rev. Lett. **116**(9), 097204 (2016).

[15]J. Xiao, G. E. W. Bauer, K. Uchida, E. Saitoh, and S. Maekawa, "Theory of magnon-driven spin Seebeck effect," Phys. Rev. B **81**(21), 214418 (2010).

[16]K. Uchida, J. Xiao, H. Adachi, J. Ohe, S. Takahashi, J. Ieda, T. Ota, Y. Kajiwara, H. Umezawa, H. Kawai, G. E. W. Bauer, S. Maekawa, and E. Saitoh, "Spin Seebeck insulator," Nat. Mater. **9**(11), 894–897 (2010).

[17]D. Meier, D. Reinhardt, M. van Straaten, C. Klewe, M. Althammer, M. Schreier, S. T. B. Goennenwein, A. Gupta, M. Schmid, C. H. Back, J.-M. Schmalhorst, T. Kuschel, and G. Reiss, "Longitudinal spin Seebeck effect contribution in transverse spin Seebeck effect experiments in Pt/YIG and Pt/NFO," Nat. Commun. **6**(1), 8211 (2015).

[18]D. Hirobe, M. Sato, T. Kawamata, Y. Shiomi, K. Uchida, R. Iguchi, Y. Koike, S. Maekawa, and E. Saitoh, "One-dimensional spinon spin currents," Nat. Phys. **13**(1), 30–34 (2017).

[19]S. Singh, M. Yarali, S. Shervin, V. Venkateswaran, K. Olenick, J. A. Olenick, J.-H. Ryou, and A. Mavrokefalos, "Temperature-dependent thermal conductivity of flexible yttria-stabilized zirconia substrate via 3ω technique," Phys. Status Solidi A **214**(10), 1700069 (2017).

[20]R. W. Powell, C. Y. Ho, and P. E. Liley, "Thermal conductivity of selected materials," Standard No. NSRDS-NBS 8 (U.S. Department of Commerce: National Bureau of Standards, 1966).

[21]T. Böhnert, R. Dutra, R. L. Sommer, E. Paz, S. Serrano-Guisan, R. Ferreira, and P. P. Freitas, "Influence of the thermal interface resistance on the thermovoltage of a magnetic tunnel junction," Phys. Rev. B **95**(10), 104441 (2017).

[22]S.-M. Lee and D. G. Cahill, "Influence of interface thermal conductance on the apparent thermal conductivity of thin films," Microscale Thermophys. Eng. **1**(1), 47–52 (1997).

[23]J. T. Newberg, D. E. Starr, S. Yamamoto, S. Kaya, T. Kendelewicz, E. R. Mysak, S. Porsgaard, M. B. Salmeron, G. E. Brown, A. Nilsson, and H. Bluhm, "Formation of hydroxyl and water layers on MgO films studied with ambient pressure XPS," Surf. Sci. **605**(1), 89–94 (2011).

[24]H.-K. Lyeo and D. G. Cahill, "Thermal conductance of interfaces between highly dissimilar materials," Phys. Rev. B **73**(14), 144301 (2006).

[25]R. Fletcher, "The Nernst-Ettingshausen coefficient and the Kondo effect in copper and gold," Philos. Mag. A **25**(1), 87–95 (1972).

[26]J. H. Mangez, J. P. Issi, and J. Heremans, "Transport properties of bismuth in quantizing magnetic fields," Phys. Rev. B **14**(10), 4381–4385 (1976).

[27]K. Behnia, M.-A. Méasson, and Y. Kopelevich, "Nernst effect in semimetals: The effective mass and the figure of merit," Phys. Rev. Lett. **98**(7), 076603 (2007).

[28]K. Behnia, "The Nernst effect and the boundaries of the Fermi liquid picture," J. Phys.: Condens. Matter **21**(11), 113101 (2009).

[29]K. Behnia and H. Aubin, "Nernst effect in metals and superconductors: A review of concepts and experiments," Rep. Prog. Phys. **79**(4), 046502 (2016).

[30]M. Kockert, R. Mitdank, A. Zykov, S. Kowarik, and S. F. Fischer, "Absolute Seebeck coefficient of thin platinum films," J. Appl. Phys. **126**(10), 105106 (2019).

[31]J. P. Moore and R. S. Graves, "Absolute Seebeck coefficient of platinum from 80 to 340 K and the thermal and electrical conductivities of lead from 80 to 400 K," J. Appl. Phys. **44**(3), 1174–1178 (1973).